Bistable Auxetic Surface Structures

TIAN CHEN, EPFL, Switzerland
JULIAN PANETTA, UC Davis, United States
MAX SCHNAUBELT, TUM, Germany
MARK PAULY, EPFL, Switzerland

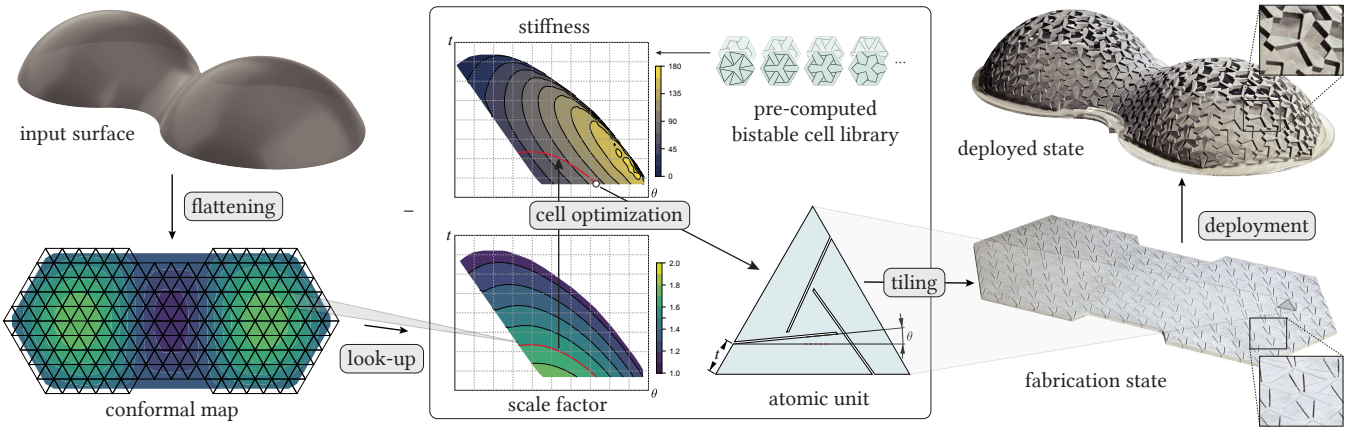

Fig. 1. Given an input target surface, our inverse design algorithm first computes a conformal flattening to the plane. We superimpose a regular tiling of user-selected resolution and integrate the local scale factor for each unit cell to serve as an index into a precomputed library of bistable auxetic cells. From all the cells with the required scale factor, we find the one with highest stiffness in the second bistable state. These cells are combined into the flat fabrication state of our deployable structure that can be laser-cut from sheet material. Actuation of the bistable cells then deploys the surface to the stable target state.

We present *Bistable Auxetic Surface Structures*, a novel deployable material system based on optimized bistable auxetic cells. Such a structure can be flat-fabricated from elastic sheet material, then deployed towards a desired double-curved target shape by activating the bistable mechanism of its component cells. A unique feature is that the deployed model is by design in a stable state. This facilitates deployment without the need of complex external supports or boundary constraints.

We introduce a computational solution for the inverse design of our Bistable Auxetic Surface Structures. Our algorithm first precomputes a library of bistable auxetic cells to cover a range of in-plane expansion / contraction ratios, while maximizing the bistability and stiffness of the cell to ensure robust deployment. We then use metric distortion analysis of the target surface to compute the planar fabrication state as a composition of cells that best matches the desired deployment deformation. As each cell expands or contracts during deployment, metric frustration forces the surface towards its target equilibrium state. We validate our method with several physical prototypes.

Authors' addresses: T. Chen, EPFL, tian.chen@epfl.ch; J. Panetta, UC Davis, jpanetta@ucdavis.edu; M. Schnaubelt, TUM, max.schnaubelt@tum.de; M. Pauly, EPFL, mark.pauly@epfl.ch.

0730-0301/2021/8-ART1 $15.00
https://doi.org/10.1145/3450626.3459940

CCS Concepts: • **Computing methodologies** → **Shape modeling**; **Modeling and simulation**.

Additional Key Words and Phrases: bi-stability, auxetic material, physics-based simulation, numerical optimization, computational design

ACM Reference Format:
Tian Chen, Julian Panetta, Max Schnaubelt, and Mark Pauly. 2021. Bistable Auxetic Surface Structures. *ACM Trans. Graph.* 40, 4, Article 1 (August 2021), 9 pages. https://doi.org/10.1145/3450626.3459940

1 INTRODUCTION

Large-scale shape transformation is crucial in many applications across different length scales, ranging from encapsulation and release of medicine [Shim et al. 2012] to the construction of space structures [Miura 1985]. In particular, structures that can deploy from a flat state to a desired target geometry can significantly reduce the time and cost of fabrication, transport, and construction [Adrover 2015]. In extreme environments such as outer space or the deep sea, deployable structures are often the only feasible means of erection.

Traditional deployable structures often employ regular periodic patterns to simplify fabrication and achieve deployment through the application of specifically designed boundary constraints. Examples of this type of structures include grid shells, cable nets, inflatable domes or deployable solar panels [Fenci and Currie 2017]. Shape control through boundary constraints is inherently limited, however, and typically leads to a narrow range of possible shapes.

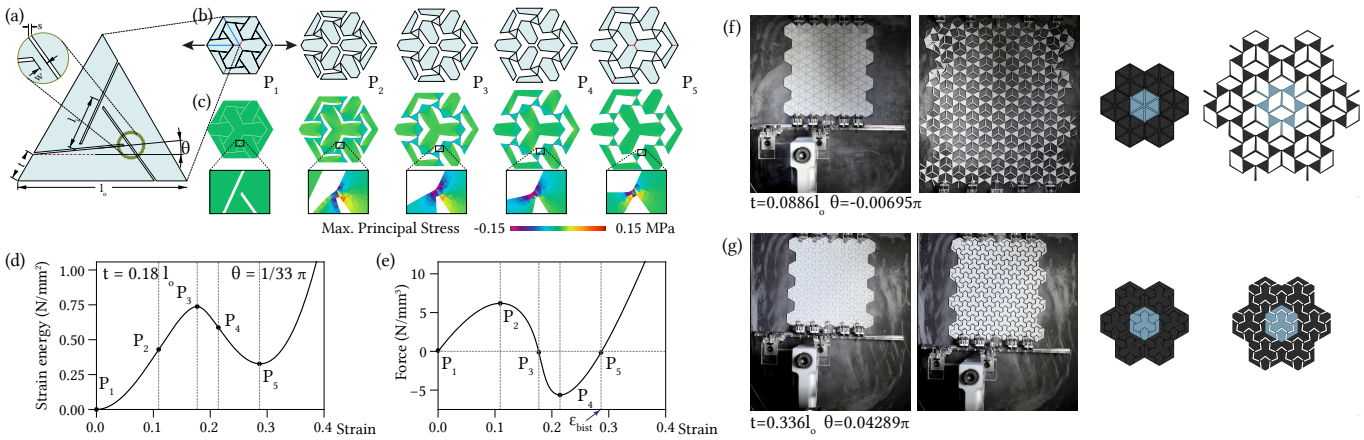

Fig. 2. Our bistable hexagonal cell is composed of six triangular units (a), each parameterized by a width t and an angle θ. When expanding the cell, triangle units become kinematically inconsistent (b), introducing strain into the cell. FE simulation in (c) illustrates the stress concentration in the compliant hinge joints connecting the rotating inner triangle elements as a result of this strain. The strain energy (d) and force (e) as a function of strain exhibit the typical bistable behavior. At the 2nd minimum of energy and zero force, the cell assumes a stable state P_5. In (f,g) we show experimental validation for two cells with different parameter settings for (t, θ).

To achieve more complex target shapes, recent work has leveraged advanced manufacturing technology to embed knowledge of the target shape into the material system itself. This shifts the complexity from the boundary to the interior of the structure and often enables a simplified, global deployment. Researchers have also incorporated smart materials that react to certain environmental conditions to achieve autonomous shape change. Typically, smart materials such as shape memory polymers, liquid crystal elastomers and artificial hydrogels are fabricated in one state, and when exposed to a trigger, transform to a second state.

Contributions. In our work we propose a novel mechanics-based solution to achieve stable shape transformation and deployment. We leverage two key principles to solve this challenging problem, namely (i) deployment of a planar surface by spatially varying isotropic expansion [Konaković-Luković et al. 2018], and (ii) auxeticity with tunable mechanical bistability [Rafsanjani and Pasini 2016]. We introduce a parameterized bistable cell that offers a continuous range of extensibility at a second stable equilibrium state through geometric variation. We show how a tiling of such cells can be optimized to program the required metric frustration into a planar sheet such that the structure globally deploys into a desired target surface and remains stable after deployment forces are removed. Our computational method is validated through scanned physical prototypes and mechanical testing.

2 RELATED WORK

We focus our discussion of previous work on deployable structures that we categorize into three classes. Our classification is based on they way the target shape is encoded, and whether deployment requires external actuation or is intrinsic in the material system. For a broader perspective on fabrication-aware computational design, we refer to recent surveys [Bermano et al. 2017; Pietroni et al. 2019].

Extrinsic deployment of regular structures. Traditional deployable structures such as pure kinematic mechanisms, gridshells and cablenets achieve their target shape through the application of external boundary constraints [Adrover 2015]. More recently, Konaković et al. [2016] studied regular linkage-based auxetic materials and established a connection to conformal geometry to define an inverse design algorithm. Garg et al. [2014] use Chebyshev nets to approximate a given target shape with a wiremesh surface. These structures have a periodic architecture, and as such encode no knowledge of the target shape, requiring external guides to deform the planar fabrication state. The inherent mechanical characteristics are taken as constants that cannot be tuned.

Extrinsic deployment of programmed structures. With the advent of powerful computational methods and digital manufacturing, we are able to design and fabricate structures whose internal architecture and/or global topology can be optimized for given input target shapes. Friedrich et al. [2018]; Konaković-Luković et al. [2018] extend auxetic linkages with locally adapted cells to allow deployment of the planar material to the target 3D shape using overpressure or gravity.

With *Flexmaps*, [Malomo et al. 2018] decompose the target surface into panels whose stiffnesses are tuned with parametrized spiral patterns to achieve the desired curvature when appropriate boundaries constraints are imposed.

Origami features customized crease lines and dihedral angles to form 3D shapes [Demaine and O'Rourke 2008]. Tachi [2009] utilizes tuck modules to approximate input polyhedral surfaces using flat sheets, where the excess material is folded beneath the surface. To ensure stability in the folded state, plasticity is inherently present across the crease lines [Shi et al. 2017]. A related construction of introducing slits within an otherwise continuous material (*a.k.a.* Kirigami) has been shown to produce sheets that deploy out-of-plane when certain boundary points are pulled [Celli et al. 2018].

X-shells [Panetta et al. 2019] and geodesic gridshells [Pillwein et al. 2020] exploit length incompatibilities within a biaxial grid-shell that, when expanded, deploys into a double-curved target shape. When the pulling forces are released, the deployed shape will close again in absence of plastic deformation or boundary constraints. Siéfert et al. [2019] introduce *biomorphs*, elastomeric materials with embedded air channels that can be inflated to generate double curvature. This deformation behavior is abstracted as an anisotropic change in the surface metric.

For material systems in this category, maintaining the structure in its target shape generally requires either active deployment forces (*e.g.*, over-pressure), whose removal would lead to structural collapse, or plastic deformation that is typically irreversible.

Intrinsic deployment of programmed structures. The last category of deployable structures embeds both the knowledge of the target shape and a means of deployment within the planar surface. These works share a unique property that energy is only needed during deployment as a trigger. Once deployed, the structure is in a state of self-equilibrium.

By fabricating an optimized layout on a pre-stretched substrate and releasing this stretch to apply a contractive force, a number of complex shapes have been demonstrated [Guseinov et al. 2017; Pérez et al. 2017]. In these works, while the deployed shapes are stable, the flat states are generally not.

A large body of work utilizes smart materials that change shape through an environmental trigger. Gladman et al. [2016]; Raviv et al. [2014] print artificial hydrogel with optimized alignments and utilize anisotropic swelling to achieve shape deployment. Multimaterial 4D printing is used in [Boley et al. 2019] to transform lattices through thermal expansion and contraction. 3D printed shape memory polymers are used for the deployment from a planar fabrication state [Ge et al. 2013], with applications for a solar panel shown in [Chen et al. 2019]. Liquid crystal elastomers with optimized nematic alignment are used to achieve shape deployment when exposed to heat or light [Aharoni et al. 2014, 2018; Kotikian et al. 2018]. Guseinov et al. [2020] additionally integrate temporal control to ensure collision-free deployment of shell structures. They employ a data-driven approach to solve the inverse design problem.

The above systems often require sophisticated fabrication technologies and custom-synthesized base materials. The necessary triggering conditions, such as exposure to large changes in temperature or humidity, can further limit the applicability of some of these systems.

Bistable mechanism. In our work, we exploit multiple equilibrium states of mechanical bistability. Bistable mechanical systems are traditionally associated with buckling and catastrophic collapse. Recently however, the nonlinearity inherent in multi-stable systems have been exploited to achieve useful functions. Bharaj et al. [2018] introduce metamorphs, planar spring-based linkage mechanisms that can transition between two pre-defined shapes. Chen et al. [2017] demonstrate 3D printed planar quadrilateral tiled surfaces that feature bistable elements to enable out-of-plane deployment. Rafsanjani and Pasini [2016] have shown a surface with periodic bistable units that also possess a Poisson's ratio of -1 at any stretch between the first and the second equilibria. In our work, we focus on eliminating the need for a continual energy input to maintain the deployed shape. Our bistable auxetic structures not only guide the deployment towards the target shape, but also favor the target surface as a local energy minimum. Thereby, energy input is only needed during deployment or un-deployment. We see our work as a first demonstration of an inverse generative algorithm for the stable out-of-plane deployment of surfaces.

3 METHOD OVERVIEW

The key principle of deployment in our approach is metric frustration. By programming variable in-plane expansion into a flat sheet of elastic material, we obtain a double-curved surface as the equilibrium state with low elastic energy that respects the new surface metric. Unique to our approach, we populate the flat sheet with bistable cells that offer controlled isotropic expansion at their second stable states, while providing sufficient resistance to the material's elastic restoring forces in the deployed state. The resulting surface is globally stable and requires no external forces to maintain its shape.

Figure 1 provides an overview of our computational inverse design approach. In a precomputation stage, we build a library of bistable auxetic cells optimized for a maximal range of expansion factors, sufficient energy barrier between the two stable states, and high stiffness in the deployed configuration. The design optimization stage then follows the approach of [Konaković-Luković et al. 2018] to first compute a conformal flattening of the design surface using the method of [Sawhney and Crane 2017]. The scale factors from this conformal map determine the pointwise in-plane expansion needed to encode the shape. A regular equilateral triangular mesh of a user-chosen resolution is overlaid on the flattened surface. We calculate the per-cell expansion factors by averaging the conformal scale factor over the area of the cell.

These expansion factors are used to query our library for the optimal bistable cells, which are then tiled to obtain the planar layout of the fabrication state. Finally, the fabricated model is actuated by pushing all cells toward their second stable state to yield the globally stable deployed surface.

4 PARAMETRIC BISTABLE CELL

The design of our parametric cell is guided by several requirements. In particular, cells should (i) exhibit bistability and sufficient stiffness in the deployed state, (ii) cover a large range of expansion factors, and (iii) seamlessly tile the plane in the fabrication state. Our parameterized cell is inspired by the auxetic bistable tilings proposed in [Rafsanjani and Pasini 2016]. Auxetic materials are materials with negative Poisson's ratio, *i.e.* when stretched in one direction, they expand also in the perpendicular directions. We specifically work with cells that can be abstracted as a one degree-of-freedom kinematic linkage with Poisson's ratio of -1, meaning they strongly resist all deformations except uniform expansion [Konaković et al. 2016]. This isotropic expansion behavior means the pattern's properties can be fully characterized by experiments stretching it along a single axis. We quantify the magnitude of this stretch with the first entry of the finite *Biot strain* tensor, which for an isotropically scaling

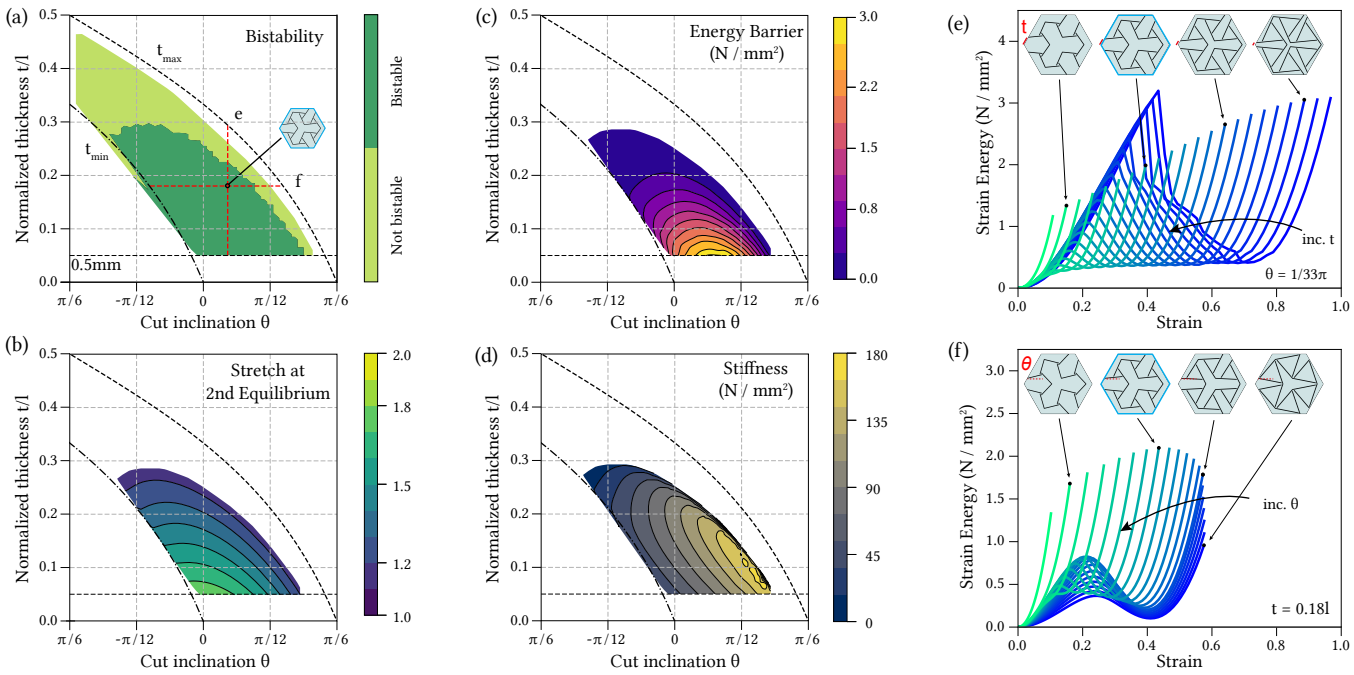

Fig. 3. Parameter sweep on our hexagonal cells. We only retain the portion of the parameter space that yields bistable cells (a). The local expansion factor covers a range of 1.129 to 1.775 (b). The energy barrier measures the difference between the minimum and maximum strain energy (c). Stiffness is evaluated with Equation 2 (d). We show the behavior of cells for a specific constant value of θ (e) and t (f), as indicated by the red vertical and horizontal lines in (a). The specific cell shown in (a) is highlighted in (e,f) in cyan (second from left).

pattern like ours, directly measures the relative length change; this quantity is the scalar-valued strain ε used throughout the paper.

Cell geometry. We define a hexagonal cell with a triangular atomic unit as illustrated in Fig. 2. All hexagons are regular with the same edge length l_o to ensure tileability. The geometry of each triangular unit within the hexagonal cell, also with an edge length of l_o, is generated using two tunable parameters, an angle θ and a thickness t. In this way we unify several geometric parametrizations proposed by [Rafsanjani and Pasini 2016] to allow for a larger design space. In addition, we have fabrication- and material-related parameters that are held constant in our analysis. In our experiments, cells are fabricated by perforating the cut lines using a CNC laser. The diameter of the laser determines the perforation width $s = 0.125$ mm. The hinge thickness $w = 0.25$ mm is empirically chosen to be as small as possible while still ensuring robustness over multiple opening-and-closing cycles of the cells.

Cell kinematics. The auxetic deformation behavior emerges due to the rotation of the embedded inner triangles of edge length l_i as the cell expands (Fig. 2). Previous works on deployable auxetics model this behavior using a purely kinematic approach with idealized point hinges (assuming $s = w = 0$) and rigid elements [Friedrich et al. 2018; Konaković et al. 2016; Konaković-Luković et al. 2018]. Bistability is defined as the existence of a second local minimizer $\varepsilon_{\text{bist}} > 0$ in the strain energy landscape (Fig. 2e). In our setting, the bistable functionality of the cell critically depends on the elasticity of the underlying material [Rafsanjani and Pasini 2016]. As shown in Fig. 2b, incompatibilities between the unit triangles suggest that when the cell is stretched, strain energy is accumulated in the intermediate states between the two stable states P_1 (at $\varepsilon = 0$) and P_5 (at $\varepsilon = \varepsilon_{\text{bist}}$). Accurately quantifying the energy barrier between these states and the stiffness around P_5 requires a physical simulation of the finite elastic deformation behavior. To determine approximately how far the simulation must stretch the cell to reach this second stable state, we derive an analytical estimate of $\varepsilon_{\text{bist}}$ based on kinematics. We derive in Appendix II an expression for the inner triangle length l_i in terms of the pattern parameters and calculate the bistable strain estimate as

$$\varepsilon_{\text{bist}} \approx \frac{2}{l_o} l_i \sin\left(\theta + \frac{\pi}{6}\right).$$

Numerical simulation. We use nonlinear periodic homogenization [Nakshatrala et al. 2013] to characterize the mechanical properties of our bistable auxetic cut patterns. To analyze a particular pattern, we simulate how a large (theoretically infinite) periodic tiling of cells behaves when stretched. We make two assumptions to simplify the simulation: (i) the tiling remains planar throughout the deformation, and (ii) the deformation does not break translation symmetry, so all repetitive units of the tiling will experience the same deformation. Note that while our patterns are defined by a chiral triangular atomic unit, we perform our simulation using a larger hexagonal cell (Fig. 3) that tiles the plane with only translations as opposed to translations and reflections.

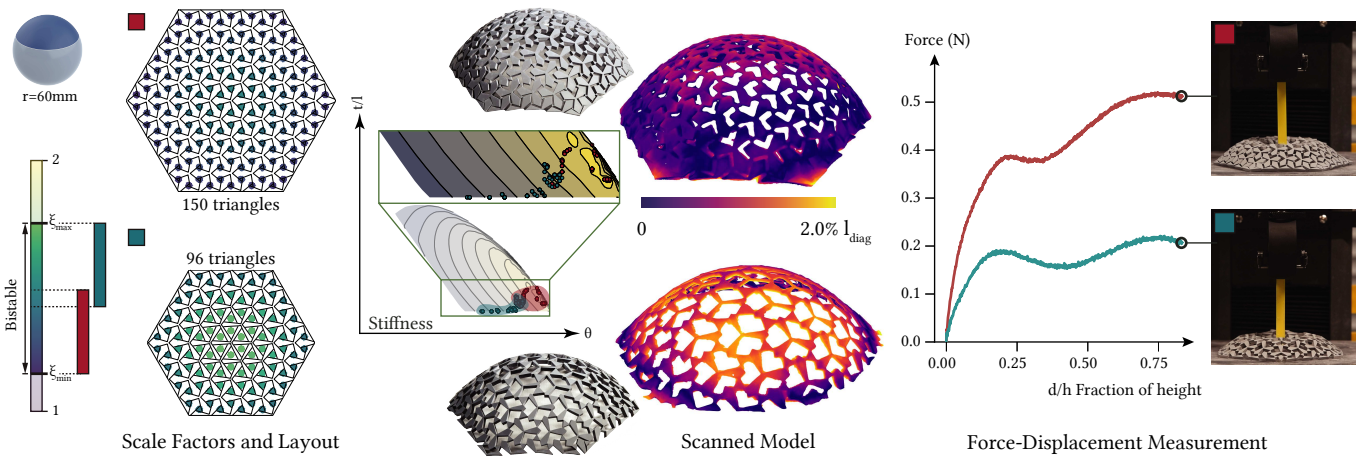

Fig. 4. A deployable spherical caps, realized at different scale factor ranges. The top row shows a model with the smallest possible expansion factors, leading to a denser and stiffer deployed shape, but requiring a larger material patch. In the bottom row, we show the smallest possible fabrication state, leading to more porous deployed state with lower stiffness. The force-displacement curve on the right is measured by applying a vertical displacement at the apex.

A kinematic analysis of the idealized linkage shows both of these assumptions are valid for the expanded state, thus we expect our simulation to accurately predict properties around the second stable state. These assumptions do mean that we over-estimate the energy barrier of cells that prefer to buckle into symmetry-breaking or out-of-plane configurations at intermediate states (this can be seen in the accompanying video). However, as discussed in Section 4, practical considerations lead us to prefer the stiffness criterion for cell selection, so any inaccuracies in the energy barrier estimate do not influence our design process.

The first assumption allows us to simulate the hexagonal cell with a 2D elasticity model defined by an energy density function $\psi : \mathbb{R}^{2\times 2} \to \mathbb{R}$ operating on 2D deformation gradients. We use a plane stress neo-Hookean membrane energy with Poisson's ratio 0.45. We note that the Young's modulus selected for the sheet material does not influence the expansion ratio and merely applies a global scaling to all energy barriers and stiffnesses. We repeated our characterizations using a lower Poisson's ratio of 0.30 and concluded that, as expected, the sheet material's Poison's ratio has negligible influence on expansion ratios and stiffnesses; a tilings' properties are almost purely a function of its unit cell geometry.

The second assumption of translational symmetry forces the deformed position of each material point $\mathbf{x}$ to take the form $\boldsymbol{\omega}(\mathbf{x}) + F\mathbf{x}$, where F is the average deformation gradient experienced by the tiling, and $\boldsymbol{\omega}$ is a displacement field that is periodic over the hexagonal tiling (commonly referred to as a *fluctuation displacement*). Accordingly, the elastic energy stored in a deformed cell Ω is given by:

$$\mathcal{E}[\boldsymbol{\omega}, F] = \int_\Omega \psi(\nabla\boldsymbol{\omega} + F)\, \mathrm{d}x.$$

We discretize this energy using quadratic finite elements (obtaining a discrete energy $E(\mathbf{w}, F) := \mathcal{E}[\sum_i w_i \boldsymbol{\phi}_i, F]$ with vector-valued shape functions $\boldsymbol{\phi}_i$), and impose the periodicity condition on $\boldsymbol{\omega}$ by assigning periodically identified mesh nodes the same displacement variables in $\mathbf{w}$. We account for the rotational invariance of the material response by restricting our consideration to *symmetric* F (*i.e.*, the stretching part of the polar decomposition of an arbitrary average deformation gradient).

Our mechanical characterization comprises two stages. In the first stage, we incrementally stretch the tiling horizontally until reaching a uniaxial strain slightly exceeding our analytic prediction of $\varepsilon_{\text{bist}}$. For each strain ε in this sequence, we simulate the tiling's deformation by solving for the minimum energy configuration:

$$E^*(\varepsilon) = \min_{\substack{F,\mathbf{w} \\ F_{00}=1+\varepsilon}} E(\mathbf{w}, F) := E(\mathbf{w}^*(\varepsilon), F^*(\varepsilon)). \tag{1}$$

The solution to this minimization problem tells us the elastic energy stored in each hexagonal cell of the tiling as well as the effective macroscopic stretch of the full tiling, $F^*(\varepsilon)$, from which we can verify the uniform expansion behavior ($F^* \approx \varepsilon I$). By recording the energy at each increment, we detect bistability with high accuracy by analyzing the energy-strain curve (*e.g.*, Fig. 2d).

In the second stage, we release the constraint on F_{00} and rerun the energy minimization, allowing the tiling to settle into an *unconstrained* local minimum at its second stable state P_5. We can then accurately measure $\varepsilon_{\text{bist}} = F^*_{00} - 1$ and calculate pattern stiffness using the following analytical formula (see Appendix I):

$$\frac{\mathrm{d}^2 E^*}{\mathrm{d}\varepsilon^2}(\varepsilon_{\text{bist}}) = \frac{\partial^2 E}{\partial F_{00}\partial \mathbf{w}}\frac{\mathrm{d}\mathbf{w}^*}{\mathrm{d}\varepsilon} + \frac{\partial^2 E}{\partial F_{00}\partial F} : \frac{\mathrm{d}F^*}{\mathrm{d}\varepsilon}. \tag{2}$$

The results of this stiffness calculation for all analyzed patterns are visualized in Fig. 3. For very weakly bistable structures, the minimization in the second stage could tunnel through the energy barrier to the undeformed state. However, this is unlikely to occur with our solver, and we found no instances where our high resolution energy-strain curves detected bistability but the second stage failed to find $\varepsilon_{\text{bist}} > 0$. Furthermore, weakly bistable structures structures like these are unfavorable for our application and would be discarded by our cell selection anyway.

We evaluate all integrals with exact Gaussian quadrature and solve the nonlinear minimization Eq. 1 with a custom Newton solver employing a standard backtracking line search and a simple Hessian modification strategy to guarantee convergence to a minimum. Solving each parametric combination takes on average 20 seconds on a PC with 2.5GHz dual-core Intel Core i7 and 16GB of RAM.

Figure 2d shows the energy landscape along the uniform expansion deployment path computed by our physical simulation for a typical hexagonal cell. The force-strain curve (Fig. 2e) can be plotted using the formula $\frac{\mathrm{d}E}{\mathrm{d}\varepsilon}$ in the appendix I. We compute the energy barrier by subtracting the energy calculated at stationary points P_3 and P_5.

Parameter Sweep. We perform a dense parameter sweep on t and θ, running our periodic simulation on each sampled cell design to evaluate the expansion factor, bistable energy barrier, and stiffness around the deployed state. We derive the parameter bounds from geometric considerations. Specifically, we aim to derive a range of geometrically feasible values of t for every feasible θ. The angle θ is constrained to lie between $\pm\frac{\pi}{6}$. Smaller values would result in cells with a different deformation mechanism that is not bistable. Larger θ would require a negative value for t. For a given θ, we can determine the bounds for t using equations derived in Appendix II. At $t = t_{\max}$, the inner triangle would vanish, and at $t = t_{\min}$, the inner triangle would occupy the entire triangular unit. The artificial limit of $t \geq 0.5\,\mathrm{mm}$ is imposed due to limits of fabrication precision.

To build our cell library, we sample θ at 43 evenly spaced values. For each θ, we sample t in increments of 0.01 mm between $t_{\min}$ and $t_{\max}$. Figure 3 summarizes the results. We observe that not all theoretically bistable cells are in fact bistable when the finite elasticity of the hinges is considered (Fig. 3a). Similarly, the achievable expansion factor (defined as $\varepsilon + 1$) does not extend to the entire theoretical range of 1 to 2 as shown in Fig. 3b.

In Fig. 2f,g, we validate our computational exploration with physical experiments to confirm the accurate prediction of the computed cell geometries. We provide all data of the cell library in supplemental material.

Cell selection. For a given target expansion factor, we can search along the corresponding isoline to find the triangular unit with the highest stiffness (see also Fig. 1) or highest energy barrier. Qualitatively, a larger energy barrier suggests that more work is required to move between two equilibrium states, whereas a higher stiffness at $\varepsilon_{\text{bist}}$ suggests that the second equilibrium is more stable, resulting in a higher-precision encoding of the expansion factor. Experimentally, we found the prototypes easier to deploy than to flatten even for patterns with relatively low energy barrier: during deployment, a cascading motion is observed where opening one cell causes its neighbours to open [Jin et al. 2020]. The opposite is true during flattening, where multiple cells must be held closed simultaneously to ensure they do not "pop" back open. This suggests that global collapse is unlikely to occur, and we should perform triangular unit selection based on stiffness to maximize the stability and accuracy of the deployed shape.

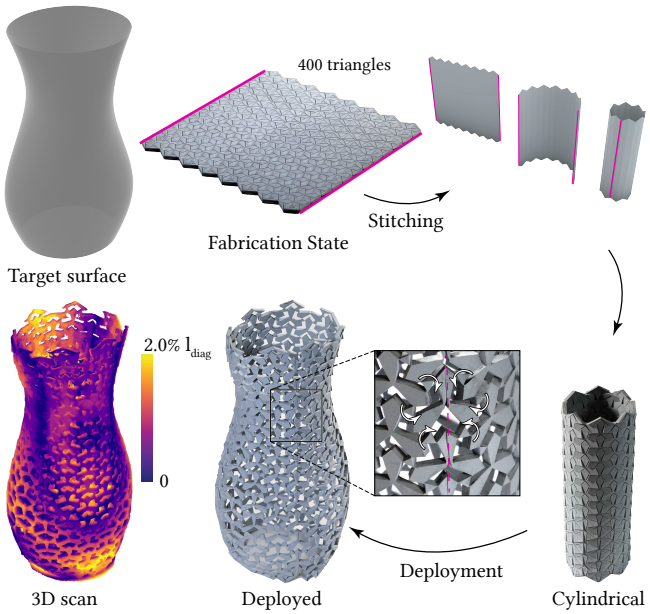

Fig. 5. This vase has been reconnected with glue along the boundary marked in red prior to deployment.

5 EVALUATION

Given the precomputed cell library, we calculate the fabrication state for a given target deployed surface as discussed in Section 3. Figures 4 to 7 show example designs created with this approach. We provide the cut patterns for all models in the supplemental material.

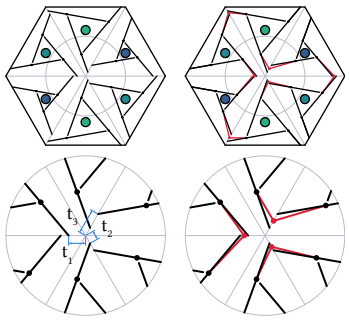

When triangular units are tiled, a mismatch is observed where the t parameters of neighboring units differ. A simple averaging operation is performed on every pair of neighboring units to match the end points of the cut lines along the boundary of the triangles as shown in the inset. For the designs shown, due to the smoothness of the scaling factor field, this adjustment is imperceptible.

Our models have been laser cut from 2.3 mm thick rubber sheets. Pushing and stretching the material manually deploys the structure to its stable target state. Due to the bistability of the cells, this deployment does not require any specific order or coordination. As soon as some cells are deployed towards their second stable state, the cascading effect propagates the deployment to the remaining structure, leading to a simple and very robust deployment procedure (see also accompanying video). We scanned all deployed model using the photometric stereo method implemented in the Metashape software [Agisoft 2021]. The error plots show the deviation of the

scan from the input reference surface as a percentage of the bounding box diagonal. As the plots indicate, the accuracy of the deployed shape is high.

Using a simple spherical cap example shown in Fig. 4, we demonstrate stable deployment in the absence of boundary constraints, as well as load carry capacity. The cap is a quarter sphere, which can be conformally mapped to the plane using a range of scale factors much narrower than our bistable cells can achieve. This allows realizing the same target geometry from different fabrication states and ultimately with different mechanical behavior of the deployed structure. Using scale factors at the lower end of the available range results in a larger fabrication state, and a denser deployed surface, and vice versa. Based on the numerically predicted stiffnesses corresponding to the parameters selected for each model, it is evident that the cap featuring lower scale factors will be stiffer. This is verified in the 3D reconstruction, as the cap with larger scale factors deforms more under gravity. We also explicitly measure the force response using a typical indentation experiment for shallow spherical shells. The two caps deliver qualitatively similar response curves, yet one exhibits a higher stiffness by a factor of approximately 2. The cells do not collapse in either experiment, and the shapes recover when the indenter is removed (see video).

Apart from the simple spherical caps, we utilize the entire expansion range in all examples to demonstrate more complex target shapes. Figure 5 illustrates how we can fabricate models from a single material sheet that do not have disk topology. The required cut defines a boundary that needs to be reconnected prior to deployment. The compatible chirality of the triangles along this seam enables deployment of the connected cylindrical geometry.

In Fig. 6 we demonstrate how we can use the same methodology to employ bistable cells that are fabricated in the open state and contract towards a closed state during deployment. Similar FE simulations are performed using negative strain values to simulate the closing behavior. While a larger flat sheet is needed to achieve the same target deployment as compared to the closed-to-open cells, this type of design results in a nearly solid deployed surface. This can be advantageous in numerous applications such as satellites, where slit-like holes are invisible to some wavelengths. Figure 7 shows design studies for architectural freeform shapes that highlight the rich shape space of our bistable auxetic surface structures. For shapes that span large unsupported spaces, external factors such as gravity result in visible deformation in the geometry when deployed.

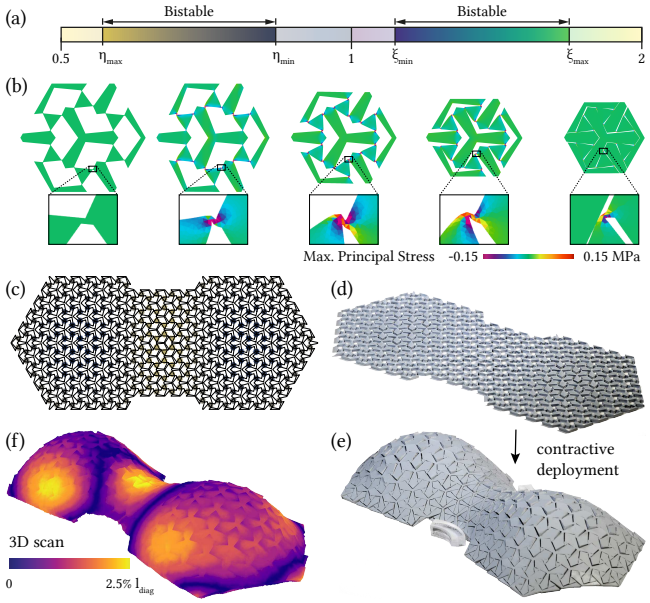

Fig. 6. Our bistable cell works both in expansion and contraction (a). In (b) we show the FE simulation of a cell in an open rest state that is contracted to a second stable state. These cells can then used in the same manner as our expansive cells for inverse design: Layout and scale factors (c), flat fabrication state (d), deployed surface (e) and error plot (f).

5.1 Limitations and Future Work

Our parametric bistable auxetic cell has a bounded isotropic expansion range, between 1.129 and 1.77 for our specific material setup. Similar to [Konaković-Luković et al. 2018], this limits the range of target shapes that we can obtain from a single sheet of material. More complex surfaces require singularities, which complicates the deployment process as cuts in the fabrication model need to be re-joined during deployment (cf. Fig. 5).

Our metric-based approach only defines the target surface up to isometry. This can necessitate additional guidance during actuation, for example to determine in which direction a convex bump should deploy; *i.e.* extrinsic curvature is not encoded in the design. In addition, surfaces that have close-to-isometric deformation modes might require additional supports to achieve a stable target state. Another drawback is that we currently do not incorporate additional physical constraints, *e.g.*, we cannot easily compensate for the effect of external forces such as gravity.

All our physical prototypes have been laser-cut from elastic sheet material. Since the key mechanism of our bistable cells is based on compliant hinge joints, this requires sufficiently flexible material to keep the bistable energy barrier, and thus actuation forces, low. At the same time, we want a sufficiently high material stiffness to keep the target state stable. The optimal trade-off is different for each base material and sheet thickness, and our cell library must be recomputed when these parameters are changed. Multi-material systems, either through monolithic additive manufacturing or assembly from components, can potentially provide more flexibility to control this trade-off.

Currently all cells in our designs are chosen to be bistable. For certain applications, we might not require a dense packing of bistable cells, but could instead mix bistable cells with other passive expansive or contractive elements. This could help increase the available scaling range and thus support a broader class of design surfaces.

As future work addressing some of the above limitations, we intend to develop an interactive tool that can inform users if an input target surface exceeds the admissible expansion range and suggest the closest feasible surface. Further, the tool would allow users to interactively specify regions of monostability and locations of topological singularities.

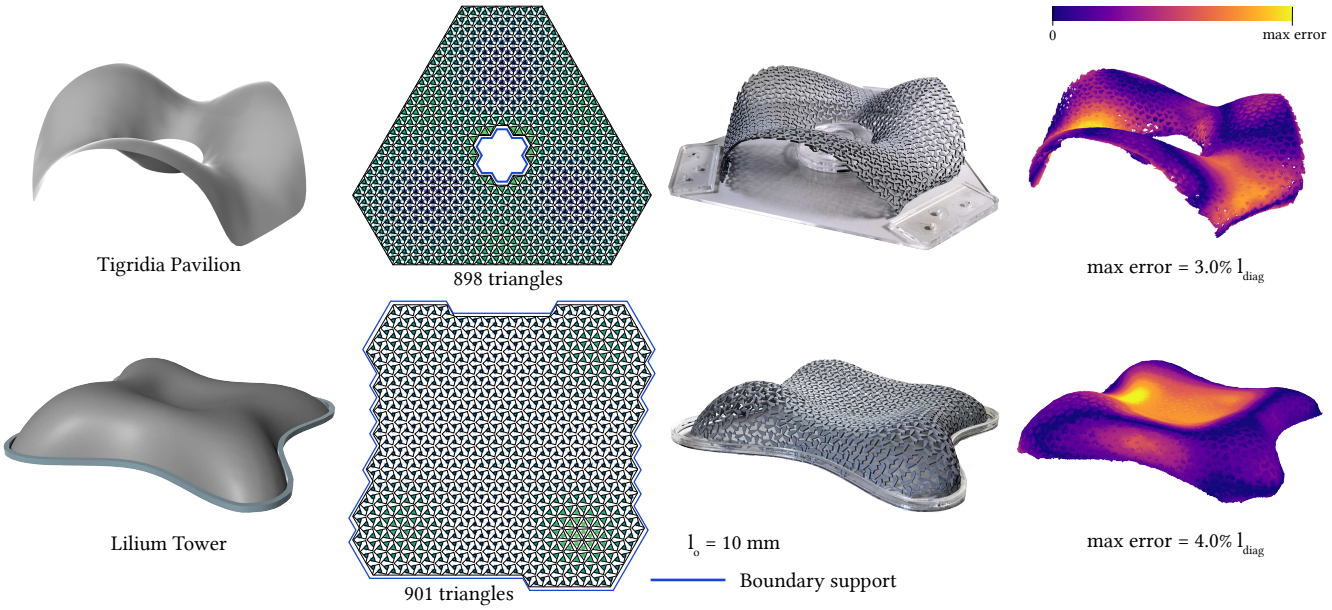

Fig. 7. Complex freeform surfaces deployed from a flat sheet. From left to right: Target surface, planar state, deployed state, deviation of scanned model.

6 CONCLUSIONS

We propose a new class of deployable surface structures composed of bistable cells that facilitate effective deployment to an implicitly encoded target shape. Deployment induces only elastic deformation and is thus reversible, yet leads to a stable target state due to the embedded bistability. One of the key benefits of our inverse design approach is simplicity. We achieve high predictive accuracy by combining local precomputation of cell behavior with global metric analysis without requiring a complex PDE-constrained global optimization to determine the cell parameters. This leads to an efficient, robust, and easy-to-use computational pipeline.

ACKNOWLEDGMENTS

We thank the anonymous reviewers for their valuable comments, and Florin Isvoranu for providing surface model of the Tigridia Pavilion. This research was supported by the NCCR Digital Fabrication, funded by the Swiss National Science Foundation (#51NF40-141853) and the SNF Award (FNS 514543 / CF 1156).

REFERENCES

Esther Rivas Adrover. 2015. *Deployable structures.* Laurence King Publishing, London.
Agisoft. 2021. Metashape, Ver. 1.7.1. https://www.agisoft.com/. Accessed: 2021-01-24.
Hillel Aharoni, Eran Sharon, and Raz Kupferman. 2014. Geometry of thin nematic elastomer sheets. *Physical review letters* 113, 25 (2014), 257801.
Hillel Aharoni, Yu Xia, Xinyue Zhang, Randall D Kamien, and Shu Yang. 2018. Universal inverse design of surfaces with thin nematic elastomer sheets. *Proc. Natl. Acad. Sci.* 115, 28 (2018), 7206–7211.
Amit H. Bermano, Thomas Funkhouser, and Szymon Rusinkiewicz. 2017. State of the Art in Methods and Representations for Fabrication-Aware Design. *Comput. Graph. Forum* 36, 2 (May 2017), 509–535.
Gaurav Bharaj, Danny Kaufman, Etienne Vouga, and Hanspeter Pfister. 2018. Metamorphs: Bistable Planar Structures. arXiv:1804.06996 [cs.GR]
J William Boley, Wim M van Rees, Charles Lissandrello, Mark N Horenstein, Ryan L Truby, Arda Kotikian, Jennifer A Lewis, and L Mahadevan. 2019. Shape-shifting structured lattices via multimaterial 4D printing. *Proc. Natl. Acad. Sci.* 116, 42 (2019), 20856–20862.
Paolo Celli, Connor McMahan, Brian Ramirez, Anton Bauhofer, Christina Naify, Douglas Hofmann, Basile Audoly, and Chiara Daraio. 2018. Shape-morphing architected sheets with non-periodic cut patterns. *Soft matter* 14, 48 (2018), 9744–9749.
Tian Chen, Osama R Bilal, Robert Lang, Chiara Daraio, and Kristina Shea. 2019. Autonomous deployment of a solar panel using elastic origami and distributed shape-memory-polymer actuators. *Physical Review Applied* 11, 6 (2019), 064069.
Tian Chen, Jochen Mueller, and Kristina Shea. 2017. Integrated design and simulation of tunable, multi-state structures fabricated monolithically with multi-material 3D printing. *Scientific reports* 7, 1 (2017), 1–8.
Erik D. Demaine and Joseph O'Rourke. 2008. *Geometric Folding Algorithms: Linkages, Origami, Polyhedra* (reprint ed.). Cambridge University Press, USA.
Giulia E Fenci and Neil GR Currie. 2017. Deployable structures classification: A review. *International Journal of Space Structures* 32, 2 (2017), 112–130.
Jan Friedrich, Sven Pfeiffer, and Christoph Gengnagel. 2018. *Locally Varied Auxetic Structures for Doubly-Curved Shapes.* Springer Singapore, Singapore, 323–336.
Akash Garg, Andrew O Sageman-Furnas, Bailin Deng, Yonghao Yue, Eitan Grinspun, Mark Pauly, and Max Wardetzky. 2014. Wire mesh design. *ACM Trans. Graph.* 33, 4 (2014), 1–12.
Qi Ge, H Jerry Qi, and Martin L Dunn. 2013. Active materials by four-dimension printing. *Applied Physics Letters* 103, 13 (2013), 131901.
A Sydney Gladman, Elisabetta A Matsumoto, Ralph G Nuzzo, Lakshminarayanan Mahadevan, and Jennifer A Lewis. 2016. Biomimetic 4D printing. *Nature materials* 15, 4 (2016), 413–418.
Ruslan Guseinov, Connor McMahan, Jesús Pérez, Chiara Daraio, and Bernd Bickel. 2020. Programming temporal morphing of self-actuated shells. *Nature communications* 11, 1 (2020), 1–7.
Ruslan Guseinov, Eder Miguel, and Bernd Bickel. 2017. CurveUps: Shaping objects from flat plates with tension-actuated curvature. *ACM Trans. Graph.* 36, 4 (2017), 1–12.
Lishuai Jin, Romik Khajehtourian, Jochen Mueller, Ahmad Rafsanjani, Vincent Tournat, Katia Bertoldi, and Dennis M. Kochmann. 2020. Guided transition waves in multistable mechanical metamaterials. *Proc. Natl. Acad. Sci.* 117, 5 (2020), 2319–2325.
Mina Konaković, Keenan Crane, Bailin Deng, Sofien Bouaziz, Daniel Piker, and Mark Pauly. 2016. Beyond developable: computational design and fabrication with auxetic materials. *ACM Trans. Graph.* 35, 4 (2016), 1–11.
Mina Konaković-Luković, Julian Panetta, Keenan Crane, and Mark Pauly. 2018. Rapid deployment of curved surfaces via programmable auxetics. *ACM Trans. Graph.* 37, 4 (2018), 1–13.
Arda Kotikian, Ryan L Truby, John William Boley, Timothy J White, and Jennifer A Lewis. 2018. 3D printing of liquid crystal elastomeric actuators with spatially programed nematic order. *Advanced materials* 30, 10 (2018), 1706164.

Luigi Malomo, Jesús Pérez, Emmanuel Iarussi, Nico Pietroni, Eder Miguel, Paolo Cignoni, and Bernd Bickel. 2018. FlexMaps: Computational Design of Flat Flexible Shells for Shaping 3D Objects. *ACM Trans. Graph.* 37, 6, Article 241 (Dec. 2018), 14 pages.
Koryo Miura. 1985. Method of packaging and deployment of large membranes in space. *The Institute of Space and Astronautical Science report* 618 (1985), 1–9.
P.B. Nakshatrala, D.A. Tortorelli, and K.B. Nakshatrala. 2013. Nonlinear structural design using multiscale topology optimization. Part I: Static formulation. *Computer Methods in Applied Mechanics and Engineering* 261-262 (2013), 167 – 176.
J. Panetta, M. Konaković-Luković, F. Isvoranu, E. Bouleau, and M. Pauly. 2019. X-Shells: A new class of deployable beam structures. *ACM Trans. Graph.* 38, 4 (2019), 1–15.
Jesús Pérez, Miguel A. Otaduy, and Bernhard Thomaszewski. 2017. Computational Design and Automated Fabrication of Kirchhoff-plateau Surfaces. *ACM Trans. Graph.* 36, 4, Article 62 (July 2017), 12 pages.
Nico Pietroni, Bernd Bickel, Luigi Malomo, and Paolo Cignoni. 2019. State of the Art on Stylized Fabrication. In *SIGGRAPH Asia 2019 Courses* (Brisbane, Queensland, Australia) *(SA '19)*. Association for Computing Machinery, New York, NY, USA, Article 118, 1 pages.
Stefan Pillwein, Kurt Leimer, Michael Birsak, and Przemyslaw Musialski. 2020. On Elastic Geodesic Grids and Their Planar to Spatial Deployment. *ACM Trans. Graph.* 39, 4, Article 125 (July 2020), 12 pages.
Ahmad Rafsanjani and Damiano Pasini. 2016. Bistable auxetic mechanical metamaterials inspired by ancient geometric motifs. *Extreme Mechanics Letters* 9 (2016), 291–296.
Dan Raviv et al. 2014. Active printed materials for complex self-evolving deformations. *Scientific reports* 4 (2014), 7422.
Rohan Sawhney and Keenan Crane. 2017. Boundary first flattening. *ACM Trans. Graph.* 37, 1 (2017), 1–14.
Yan Shi, Fan Zhang, Kewang Nan, Xueju Wang, Juntong Wang, Yijie Zhang, Yutong Zhang, Haiwen Luan, Keh-Chih Hwang, Yonggang Huang, John A. Rogers, and Yihui Zhang. 2017. Plasticity-induced origami for assembly of three dimensional metallic structures guided by compressive buckling. *Extreme Mechanics Letters* 11 (2017), 105 – 110.
J. Shim, C. Perdigou, E. R. Chen, Katia Bertoldi, and P. M. Reis. 2012. Buckling-induced encapsulation of structured elastic shells under pressure. *Proc. Natl. Acad. Sci.* 109, 16 (2012), 5978–5983.
Emmanuel Siéfert, Etienne Reyssat, José Bico, and Benoit Roman. 2019. Bio-inspired pneumatic shape-morphing elastomers. *Nature materials* 18, 1 (2019), 24–28.
T. Tachi. 2009. Origamizing Polyhedral Surfaces. *IEEE Transactions on Visualization and Computer Graphics* 16, 2 (2009), 298–311.

APPENDIX I

We provide the formulas necessary to compute a unit cell's stiffness along its 1D deployment path. First, note that the equilibrium deformation variables at a given stretch, $\mathbf{w}^*(\varepsilon)$ and $F^*(\varepsilon)$, solve the system of nonlinear equations:

$$\frac{\partial E}{\partial \mathbf{w}}(\mathbf{w}^*, F^*) = 0, \quad \frac{\partial E}{\partial F}(\mathbf{w}^*, F^*) = \begin{bmatrix} \lambda & 0 \\ 0 & 0 \end{bmatrix}, \quad F_{00} = \varepsilon \qquad (3)$$

for some unknown stretching force λ. Differentiating the energy at equilibrium with respect to strain ε yields:

$$\frac{\mathrm{d}E^*}{\mathrm{d}\varepsilon} = \frac{\partial E}{\partial \mathbf{w}}(\mathbf{w}^*, F^*)\frac{\mathrm{d}\mathbf{w}^*}{\mathrm{d}\varepsilon} + \frac{\partial E}{\partial F}(\mathbf{w}^*, F^*) : \frac{\mathrm{d}F^*}{\mathrm{d}\varepsilon} = \frac{\partial E}{\partial F_{00}}(\mathbf{w}^*, F^*),$$

where nearly all terms vanish due to Eq. 3. Differentiating a second time yields Eq. 2, for which we need the equilibrium derivatives $\frac{\mathrm{d}\mathbf{w}^*}{\mathrm{d}\varepsilon}$ and $\frac{\mathrm{d}F^*}{\mathrm{d}\varepsilon}$. Flattening the unconstrained entries of F into a vector $\mathbf{f} := [F_{01}, F_{11}]$, we find these derivatives by differentiating both sides of Eq. 3 and solving the resulting system:

$$\begin{bmatrix} \frac{\partial^2 E}{\partial \mathbf{w}^2} & \frac{\partial^2 E}{\partial \mathbf{w}\partial \mathbf{f}} \\ \frac{\partial^2 E}{\partial \mathbf{f}\partial \mathbf{w}} & \frac{\partial^2 E}{\partial \mathbf{f}^2} \end{bmatrix} \begin{bmatrix} \frac{\mathrm{d}\mathbf{w}^*}{\mathrm{d}\varepsilon} \\ \frac{\mathrm{d}\mathbf{f}^*}{\mathrm{d}\varepsilon} \end{bmatrix} = - \begin{bmatrix} \frac{\partial^2 E}{\partial \mathbf{w}\partial F_{00}} \\ \frac{\partial^2 E}{\partial \mathbf{f}\partial F_{00}} \end{bmatrix},$$

which can be assembled from the individual energy Hessian terms:

$$\frac{\partial^2 E}{\partial w_i \partial w_j} = \int_\Omega \nabla \boldsymbol{\phi}_i : \psi'' : \nabla \boldsymbol{\phi}_j \, \mathrm{d}x,$$

$$\frac{\partial^2 E}{\partial w_i \partial F} = \int_\Omega \nabla \boldsymbol{\phi}_i : \psi'' \, \mathrm{d}x, \quad \frac{\partial^2 E}{\partial F^2} = \int_\Omega \psi'' \, \mathrm{d}x.$$

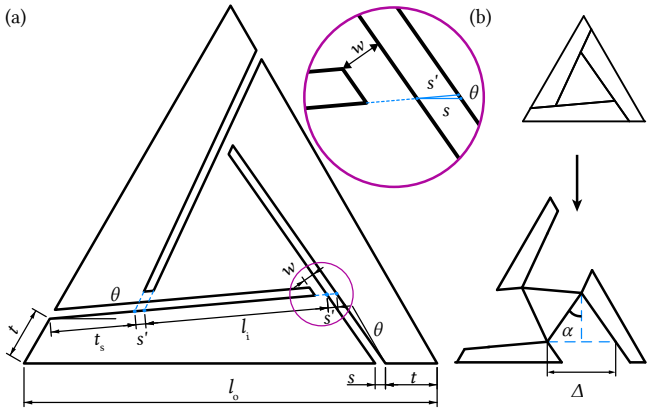

Fig. 8. The geometry of the unit cell is defined parametrically. By changing t and θ, we cover the theoretical expansion ratios between 1 and 2.

Here, ψ'' is the second derivative of membrane energy density ψ with respect to its argument, evaluated at $\nabla\boldsymbol{\omega}^* + F^*$.

APPENDIX II

We derive the quantities used in the estimation of $\varepsilon_{\text{bist}}$ in Eq. 4. First, referring to Fig. 8a, we derive expressions for l_i and t_s by formulating a system of two equations:

$$t\sin\left(\frac{\pi}{3}\right) + (t_\mathrm{s} + l_\mathrm{i} + 2s')\sin(\theta) = t_\mathrm{s}\sin\left(\frac{\pi}{3} - \theta\right),$$
$$t\cos\left(\frac{\pi}{3}\right) + (t_\mathrm{s} + l_\mathrm{i} + 2s')\cos(\theta) + t_\mathrm{s}\cos\left(\frac{\pi}{3} - \theta\right) + t = l_\mathrm{o}.$$

Solving for both t_s and l_i,

$$t_\mathrm{s} = t\cos(\theta) + \sqrt{3}\left(\frac{2l_\mathrm{o}}{3} - t\right)\sin(\theta)$$

$$l_\mathrm{i} = (l_\mathrm{o} - 3t)\cos(\theta) + \sqrt{3}(t - l_\mathrm{o})\sin\theta - 2s'.$$

We calculate the projected length s' as

$$s' = -\frac{s}{3}\left(\sqrt{3}\sin(\theta) - 3\cos(\theta)\right),$$

obtaining a final expression for l_i:

$$l_\mathrm{i} = \left(\frac{2}{3}s + t - l_\mathrm{o}\right)\sqrt{3}\sin(\theta) - (2s + 3t - l_\mathrm{o})\cos(\theta).$$

Note that w remains included in l_i and can be adjusted at will prior to fabrication. The bounds for t are found as follows: $t_{\min}$ occurs when $t_\mathrm{s} = 0$ and $t_{\max}$ occurs when $l_\mathrm{i} = 0$, i.e.,

$$t_{\min} = l_\mathrm{o}\frac{2\sin(\theta)\sqrt{3}}{3\sin(\theta)\sqrt{3} - 3\cos(\theta)},$$

$$t_{\max} = \frac{(-2s + 3l_\mathrm{o})\sqrt{3}\sin(\theta) + 3(2s - l_\mathrm{o})\cos(\theta)}{3\sqrt{3}\sin(\theta) - 9\cos(\theta)}.$$

Lastly, Eq. 4 can be derived by referring to Fig. 8b, where $\alpha = \theta + \pi/6$. The extension in length is therefore $\Delta = 2\,l_\mathrm{i}\sin(\alpha)$. The strain estimate can then be calculated as $\varepsilon_{\text{bist}} = \Delta/l_\mathrm{o}$.